Three-dimensional lattice-Boltzmann model of van der Waals fluids

A. N. Kalarakis, V. N. Burganos,* and A. C. Payatakes
Institute of Chemical Engineering and High Temperature Chemical Processes, Foundation for Research and Technology, Hellas (ICE/HT-FORTH)
and Department of Chemical Engineering, University of Patras, P.O. Box 1414, GR 265 04, Patras, Greece
(Received 7 August 2002; published 31 January 2003)

A three-dimensional lattice-Boltzmann model is developed for the simulation of nonideal fluids under static and flow conditions. The van der Waals formulation of quasilocal thermodynamics for nonuniform fluids is used, and the interfacial stress tensor for nonideal fluids appears explicitly in the hydrodynamic equations. The continuity and flow equations are fully recovered, and Galilean invariance is restored through appropriate manipulations of the pressure tensor. Although applied here to the D_3Q_{15} lattice, the methodology of Galilean restoration can be easily modified for use with other three-dimensional lattices as well. The Laplace law and Gibbs-Thomson equations are satisfied with excellent accuracy by the model, as demonstrated by droplet equilibrium simulations. Spinodal decomposition and droplet coalescence simulations are also carried out, revealing a direct proportionality of the characteristic times to the viscosity, as expected. A wettability adjustment was made possible through the prescription of a chemical potential profile along the fluid-wall interface, and used for the simulation of droplet formation from a conical orifice.

DOI: 10.1103/PhysRevE.67.016702 PACS number(s): 83.85.Pt, 68.03.Cd, 83.50.−v

I. INTRODUCTION

In a recent publication [1], the authors presented a lattice-Boltzmann (LB) approach for the modeling of vapor-liquid equilibrium and the flow of a van der Waals fluid. The interfacial phenomena of this nonideal system are captured using the free-energy approach, originally introduced in the context of LB schemes by Swift and co-workers [2,3]. A methodology for the prescription of the fluid properties in the context of such an approach was presented by Angelopoulos *et al.* [4]. The thermodynamic aspects of this model follow the van der Waals mean-field theory for nonuniform fluids [5,6]. Although the model was shown to be capable of simulating two-phase flow problems [4], the lack of Galilean invariance could lead to a reduced accuracy in the calculation of the flow field, in transient or steady-state flow simulations.

The main theoretical advance in our recent work [1] was the restoration of Galilean invariance and the concomitant recovery of the actual Navier-Stokes equation, using the two-dimensional (2D) seven-speed model. Validation of the model was implemented under static conditions, and its performance in droplet formation and flow simulations was investigated. A similar concept for Galilean invariance restoration was used by Holdych *et al.* [7] in an older publication in the 2D nine-speed model.

In the present work, a 3D lattice-Boltzmann model of nonideal fluids is developed and tested. The model is an extension of our previous 2D model to three dimensions, and uses a cubic lattice with 15 velocity vectors per cell. The van der Waals theory for nonuniform fluids is used, and a rigorous method for restoring Galilean invariance is presented. The practical need for this work arises form the large number of technological applications that involve interfacial phenomena under static or flow conditions. Although a variety of computational fluid dynamics (CFD) techniques have been developed for the solution of the Navier-Stokes equation in single and multiphase flow problems, the LB approach holds strong promise as an alternative numerical procedure on the grounds of several distinct features. A great advantage of LB models is that they can easily simulate flow with highly complicated solid or free boundaries. Especially in multiphase flow cases, LB models do not need interface tracking algorithms—unlike conventional CFD codes—and the motion and evolution of deformable bodies, including coalescence and breakup phenomena, are simulated in a straightforward fashion. A practical advantage is that LB coding is far easier than algorithms that solve the flow equation. Furthermore, LB models lend themselves naturally to parallel coding, thus taking advantage of the rapid progress in the multiprocessor computer technology that is enjoyed nowadays. Although significant progress is still to be made with thermal LB models and with high density ratio for two-phase systems, currently available two-phase flow LB approaches can provide a very useful framework for the understanding and simulation of flow phenomena that develop in classical fluid mechanics problems with and without solid boundaries (e.g., porous media). A comprehensive review of LB methods focusing on two-phase flow modeling, accuracy, applications, and current restrictions is provided by Házi *et al.* [8].

Recently, some other two-phase LB models have been extended to three dimensions using either the interacting potential approach [9,10] or the free-energy approach [11,12] proposed by Swift *et al.* [3]. The 3D model developed here is used to simulate droplet equilibrium, droplet coalescence, and vapor-liquid flow including droplet motion and deformation. This paper is organized as follows: Section II presents a 3D two-phase model, along with the necessary corrections made for Galilean invariance restoration. In Sec. III, the results of the application of the model to static and flow problems are presented, and the significance of restoring Galilean

*Corresponding author. Email address: vbur@iceht.forth.gr

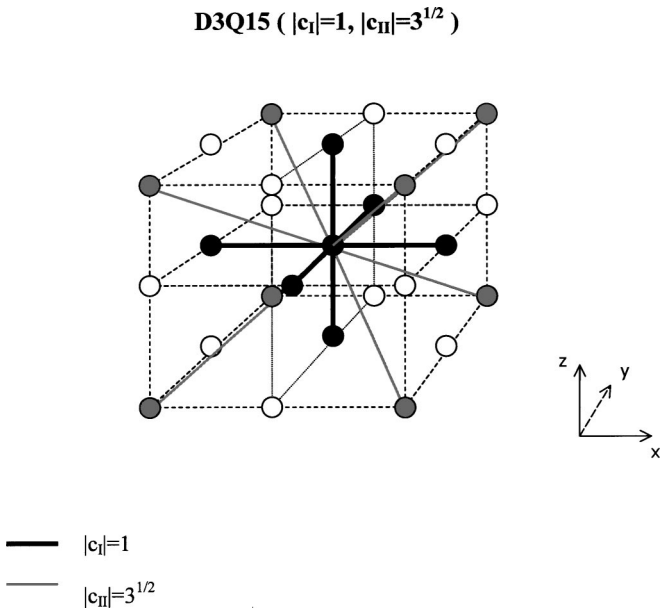

FIG. 1. Lattice geometry and unit paths assumed in the D_3Q_{15} model.

invariance is demonstrated. The main conclusions of this work are summarized in Sec. IV.

II. LATTICE-BOLTZMANN TWO-PHASE MODEL IN THREE DIMENSIONS

A. Model development

In this section the development of a three-dimensional lattice-Boltzmann model of nonideal fluids is presented. Single-particle distribution functions f_i, discrete in both time and space, are used within a particle population ensemble. The particle populations reside only on the nodes of the lattice and move along a well-defined set of unit vectors ($\underline{e}_i$), corresponding to the directions (indicated by the subscript i) of the neighboring nodes. The ensemble evolves according to the lattice-Boltzmann equation, simplified with the use of the single time relaxation approach, introduced by Bhatnagar, Gross, and Krook [13]:

$$f_{ki}(\underline{x}+\underline{e}_{ki}\Delta t,t+\Delta t)-f_{ki}(\underline{x},t)=-\frac{1}{\tau}[f_{ki}(\underline{x},t)-f_{ki}^{\mathrm{eq}}(\underline{x},t)]. \tag{1}$$

In Eq. (1) $f_{ki}^{\mathrm{eq}}(\underline{x},t)$ is the equilibrium distribution function, τ is the single relaxation time which controls the rate of approach to equilibrium, Δt is the time step, and $\underline{x}$ is the position vector. Subscript k is used to classify the particle population into subpopulations, according to their speed ($|\underline{e}_{ki}|$), namely, $k=0$ for the rest particles and $k>1$ for the mobile ones. The distribution function $f_{ki}(\underline{x},t)$ represents the probability of finding a particle at node $\underline{x}$ and time t with velocity $\underline{e}_{ki}$. In the present work the three-dimensional fcc lattice is employed, and 14 distinct directions of particle propagation at each time step are used (D_3Q_{15}) (Fig. 1). This model has the required underlying symmetry to restore the correct macroscopic equations of fluid motion [14,15]. There are two types of moving populations: populations of type 1 ($k=1$) move along the principal axes ($|\underline{e}_{1i}|=1$, $i=1,6$) and populations of type 2 ($k=2$) move along the eight diagonals ($|\underline{e}_{2i}|=\sqrt{3}$, $i=7,14$). Rest particle populations with zero speed ($k=0$) are also allowed ($|\underline{e}_0|=0$).

The local density ρ and velocity $\underline{u}$ are obtained from the first two moments of the distribution function:

$$\rho=\sum_{k,i} f_{ki}, \quad \rho\underline{u}=\sum_{k,i} \underline{e}_i f_{ki}. \tag{2}$$

The equilibrium distribution function f_{ki}^{eq} is expanded as a power series of the local velocity $\underline{u}$, up to second order, in which additional nonlocal terms are included to allow the prescription of the properties of a nonideal fluid [2]:

$$f_{ki}^{\mathrm{eq}}=A_k+B_k(\underline{e}_{ki}\cdot\underline{u})+C_k(\underline{e}_{ki}\cdot\underline{u})^2+D_k u^2 + \underline{\underline{G}}_k:\underline{e}_{ki}\underline{e}_{ki}+O(u^3). \tag{3}$$

The coefficients are determined from the local conservation rules for mass and momentum,

$$\rho=\sum_{k,i} f_{ki}^{\mathrm{eq}}, \quad \rho\underline{u}=\sum_{k,i} \underline{e}_{ki} f_{ki}^{\mathrm{eq}}, \tag{4}$$

the constraints of isotropy and Galilean invariance, the requirement that the pressure tensor be independent of the velocity, and from the zero order momentum flux tensor ($\underline{\underline{\Pi}}^{(0)}$) for nonideal fluids,

$$\Pi_{\alpha\beta}^{(0)}\equiv\sum_k \sum_i e_{ki\alpha}e_{ki\beta}f_i^{\mathrm{eq}}=P_{\alpha\beta}+\rho u_\alpha u_\beta, \tag{5}$$

where $P_{\alpha\beta}$ is the pressure tensor.
The pressure tensor for inhomogeneous fluids is [16]

$$P_{\alpha\beta}(\underline{r})=P(\underline{r})\,\delta_{\alpha\beta}+\kappa\nabla_\alpha\rho\nabla_\beta\rho. \tag{6}$$

Following the van der Waals quasi-thermodynamic theory of nonuniform fluids [5] and the Cahn-Hilliard approach [6], the diagonal terms of the pressure tensor are related to the free energy through

$$P(\underline{r})=\rho\left(\frac{\delta\Psi}{\delta\rho}\right)_T-\Psi=p_0-\kappa\rho\nabla^2\rho-\frac{\kappa}{2}|\nabla\rho|^2, \tag{7}$$

where p_0 is the pressure of the fluid which is connected to the density through the equation of state:

$$p_0=\rho\frac{\partial\psi(\rho)}{\partial\rho}-\psi(\rho), \tag{8}$$

$\Psi(\underline{r})$ is the free energy functional according to the square-gradient approximation,

$$\Psi(\underline{r})=\int\left[\frac{1}{2}m|\nabla\rho(\underline{r})|^2+\psi[\rho(\underline{r})]\right]dr, \tag{9}$$

and $\psi(\rho(\underline{r}))$ is the local free-energy density of the fluid.

The following velocity vectors are used with the D_3Q_{15} model:

$$\underline{e}_0=\underline{0}, \quad \underline{e}_{1i}=\mathrm{cycl}(\pm 1,0,0) \quad \text{for } i=1\ldots 6$$

and

$$\underline{e}_{2i}=\sqrt{3}(\pm 1,\pm 1,\pm 1) \quad \text{for } i=7\ldots 14,$$

which satisfy the identities

$$\sum_i e_{ki\alpha}=\sum_i e_{ki\alpha}e_{ki\beta}e_{ki\gamma}=0,$$

$$\sum_i e_{ki\alpha}e_{ki\beta}=\frac{bc_k^2}{D}\delta_{\alpha\beta}=\begin{cases}2\delta_{\alpha\beta}, & k=1\\ 8\delta_{\alpha\beta}, & k=2,\end{cases} \tag{10}$$

$$\sum_i e_{ki\alpha}e_{ki\beta}e_{ki\gamma}e_{ki\delta}=\frac{bc_k^4}{D(D+2)}\Delta_{\alpha\beta\gamma\delta}=\begin{cases}2\delta_{\alpha\beta\gamma\delta}, & k=1\\ 8\delta_{\alpha\beta\gamma\delta}, & k=2,\end{cases}$$

$$\Delta_{\alpha\beta\gamma\delta}=\delta_{\alpha\beta}\delta_{\gamma\delta}+\delta_{\alpha\gamma}\delta_{\beta\delta}+\delta_{\alpha\delta}\delta_{\beta\gamma}.$$

In the above, the greek subscripts represent the macroscopic x, y, and z coordinates, and $c_1=1$, and $c_2=\sqrt{3}$.

Using constraints (4) and (5) and Eqs. (10) the expansion coefficients are determined as

$$A_0=\rho-\frac{7\left(p_0-\kappa\rho\nabla^2\rho-\frac{1}{6}\kappa|\underline{\nabla}\rho|^2\right)}{3}=\rho-7A_1,$$

$$A_1=\frac{p_0-\kappa\rho\nabla^2\rho-\frac{1}{6}\kappa|\underline{\nabla}\rho|^2}{3},$$

$$A_2=\frac{p_0-\kappa\rho\nabla^2\rho-\frac{1}{6}\kappa|\underline{\nabla}\rho|^2}{24}=\frac{A_1}{8},$$

$$B_0=0, \quad B_1=\rho/3, \quad B_2=\rho/24,$$

$$C_0=0, \quad C_1=\rho/2, \quad C_2=\rho/16,$$

$$D_0=-\rho/3, \quad D_1=-\rho/6, \quad D_2=-\rho/48, \tag{11}$$

$$G_{1xx}=\frac{\kappa}{6}\left[2\left(\frac{\partial\rho}{\partial x}\right)^2-\left(\frac{\partial\rho}{\partial y}\right)^2-\left(\frac{\partial\rho}{\partial z}\right)^2\right],$$

$$G_{1yy}=\frac{\kappa}{6}\left[-\left(\frac{\partial\rho}{\partial x}\right)^2+2\left(\frac{\partial\rho}{\partial y}\right)^2-\left(\frac{\partial\rho}{\partial z}\right)^2\right],$$

$$G_{1zz}=\frac{\kappa}{6}\left[-\left(\frac{\partial\rho}{\partial x}\right)^2-\left(\frac{\partial\rho}{\partial y}\right)^2+2\left(\frac{\partial\rho}{\partial z}\right)^2\right],$$

$$G_{1xz}=\frac{\kappa}{2}\frac{\partial\rho}{\partial x}\frac{\partial\rho}{\partial z}, \quad G_{1xy}=\frac{\kappa}{2}\frac{\partial\rho}{\partial x}\frac{\partial\rho}{\partial y}, \quad G_{1yz}=\frac{\kappa}{2}\frac{\partial\rho}{\partial x}\frac{\partial\rho}{\partial z},$$

$$G_{2xx}=\frac{G_{1xx}}{8}, \quad G_{2yy}=\frac{G_{1yy}}{8} \quad G_{2zz}=\frac{G_{1zz}}{8},$$

$$G_{2xy}=\frac{G_{1xy}}{8}, \quad G_{2xz}=\frac{G_{1xz}}{8} \quad G_{2yz}=\frac{G_{1yz}}{8}.$$

Application of the Chapman-Enskog approach to the lattice-Boltzmann equation eventually results in the macroscopic mass and momentum conservation equations:

(a) mass conservation equation:

$$\frac{\partial}{\partial t}\rho+\nabla\cdot\rho\underline{u}=0, \tag{12}$$

(b) momentum conservation equation:

$$\begin{aligned}\frac{\partial}{\partial t}(\rho\underline{u})+\nabla\cdot(\rho\underline{\underline{uu}})&=-\nabla\underline{\underline{P}}+\nabla\left[\left(\frac{2\tau-1}{6}\right)\rho\{\nabla\underline{u}+(\nabla\underline{u})^T\}\right]\\&+\nabla\left[\left(\tau-\frac{1}{2}\right)\left(\frac{1}{3}-\frac{\partial P}{\partial\rho}\right)\rho(\nabla\cdot\underline{u})\right]+\nabla\left[\left(\frac{2\tau-1}{6}\right)\right.\\&\left.\times\left(1-\frac{1}{3}\frac{\partial P}{\partial\rho}\right)\{\underline{u}\nabla\rho+(\underline{u}\nabla\rho)^T\}\right]+\nabla\left[\left(\tau-\frac{1}{2}\right)\right.\\&\left.\times\left(\frac{1}{3}-\frac{\partial P}{\partial\rho}\right)(\underline{u}\cdot\nabla\rho)\right]+O(u^3).\end{aligned} \tag{13}$$

The kinematic viscosity (ν) and the bulk viscosity (κ) are given by the following expressions, respectively:

$$\nu=\frac{2\tau-1}{6}, \quad \frac{\kappa}{\rho}=\nu\left(\frac{5}{3}-3\frac{\partial P}{\partial\rho}\right). \tag{14}$$

The momentum conservation equation [Eq. (13)] contains two density gradient-dependent terms on the right-hand side that do not appear in the exact momentum equation. This discrepancy is eliminated in Sec. III, and Galilean invariance is restored. Another significant difference of Eq. (13) and the macroscopic momentum equation is the form of the gradient of the pressure tensor. According to its explicit expression given in Eq. (6), it is easy to show that the pressure tensor divergence is made up of two terms: the pressure tensor of the nonideal fluid and the stress tensor that accounts for the interfacial tension effects,

$$\nabla\cdot\underline{\underline{P}}=\nabla p_0-\nabla\cdot\underline{\underline{\Pi}}^{(s)}, \tag{15}$$

where

$$\underline{\underline{\Pi}}^{(s)}=\left(\kappa\rho\nabla^2\rho+\frac{\kappa}{2}|\nabla\rho|^2\right)\underline{\underline{\delta}}-\kappa\nabla\rho\nabla\rho. \tag{16}$$

The use of the interfacial stress tensor $\underline{\underline{\Pi}}^{(s)}$ in the momentum equation [17] was also confirmed by Zou and He [18] using kinetic theory arguments in their discrete Boltzmann equation approach.

B. Restoration of Galilean invariance

The appearance of the last two terms in the momentum equation is physically incorrect and may be responsible for the lack of Galilean invariance of the 3D LB model developed here. In order to recover the correct macroscopic momentum equation, these two terms must be eliminated. This can be achieved through a procedure that is similar to that developed by the authors in the 2D LB case [1], and consists of the appropriate incorporation of the density gradient terms into the pressure tensor. The pressure tensor can assume the following general form:

$$\sum_{k,i} f_{ki}^{\mathrm{eq}} e_{ki\alpha} e_{ki\beta} = P'_{\alpha\beta} + \rho u_\alpha u_\beta = \Big[P_{\alpha\beta} + \zeta (u_\beta \partial_\alpha \rho + u_\alpha \partial_\beta \rho) + \xi \sum_\gamma u_\gamma \partial_\gamma \rho \delta_{\alpha\beta} \Big] + \rho u_\alpha u_\beta. \tag{17}$$

In the above equation, an index notation has been used. The symbol ∂_α denotes spatial derivatives, and greek subscripts represent the macroscopic x, y, and z coordinates. Following algebraic manipulations, it can be shown that the correct momentum equation is recovered if

$$\zeta = \xi = \nu' = \nu \left(1 - 3 \frac{\partial P}{\partial \rho} \right). \tag{18}$$

Substituting the equilibrium distribution expansion [Eq. (3)] and the pressure tensor form [Eq. (6)] in Eq. (17), the coefficients of the equilibrium distribution function for the Galilean invariant model are obtained (primed quantities):

$$\begin{aligned}
A'_1 &= A_1 + \frac{5}{9} \nu' \sum_\gamma u_\gamma \partial_\gamma \rho, \\
A'_2 &= A_2 + \frac{5}{72} \nu' \sum_\gamma u_\gamma \partial_\gamma \rho = \frac{A'_1}{8}, \\
A'_0 &= A_0 - \frac{35}{9} \nu' \sum_\gamma u_\gamma \partial_\gamma \rho = \rho - 7A'_1, \\
B'_1 &= B_1, \quad B'_2 = B_2, \\
C'_1 &= C_1, \quad C'_2 = C_2, \\
D'_0 &= D_0, \quad D'_1 = D_1, \quad D'_2 = D_2, \\
G'_{1\alpha\alpha} &= G_{1\alpha\alpha} + \frac{\nu'}{2} \left(2u_\alpha \partial_\alpha \rho - \frac{2}{3} \sum_\gamma u_\gamma \partial_\gamma \rho \right), \\
G'_{2\alpha\alpha} &= G_{2\alpha\alpha} + \frac{\nu'}{16} \left(2u_\alpha \partial_\alpha \rho - \frac{2}{3} \sum_\gamma u_\gamma \partial_\gamma \rho \right) = \frac{G'_{1\alpha\alpha}}{8}, \\
G'_{1\alpha\beta} &= G_{1\alpha\beta} + \frac{\nu'}{2} (u_\beta \partial_\alpha \rho + u_\alpha \partial_\beta \rho), \\
G'_{2\alpha\beta} &= G_{2\alpha\beta} + \frac{\nu'}{16} (u_\beta \partial_\alpha \rho + u_\alpha \partial_\beta \rho) = \frac{G'_{1\alpha\beta}}{8}.
\end{aligned} \tag{19}$$

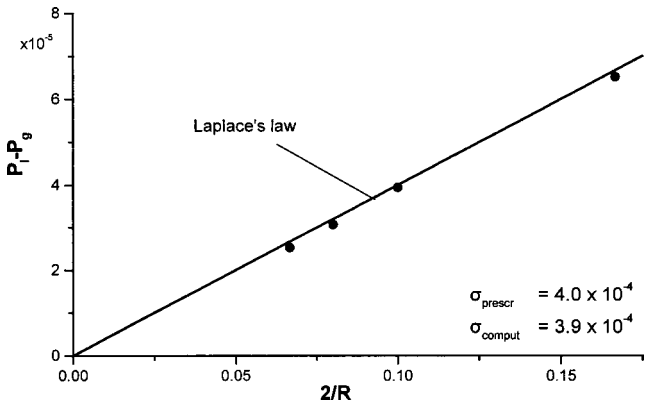

FIG. 2. Laplace law test for a 3D droplet. The solid line represents the Laplace law equation and the symbols indicate the simulation results.

III. RESULTS AND DISCUSSION

A validation of the model through comparison of simulation results to theoretical predictions is presented first. A liquid droplet in equilibrium with its surrounding vapor is simulated under static conditions and the pressure difference across the interface is calculated for various droplet sizes. The parameter values $\nu_l = \nu_g = 1.67 \times 10^{-2}$, $m = 1.8 \times 10^{-3}$, and $\rho_l = 2$, $\rho_g = 1$ are prescribed in a self-consistent way according to the algorithm proposed by Angelopoulos *et al.* [4], and are expressed in dimensionless form ("lattice Boltzmann units"). The basic reference quantities are the density of a unit cell, $\tilde{\rho}_0$, the speed of type-I particles, $\tilde{e}_0$, and the lattice constant, $\tilde{l}_0$, for the fluid density, fluid velocity, and length, respectively. The pressure is rendered dimensionless using the quantity $\tilde{\rho}_0 \tilde{e}_0^2$, the kinematic viscosity using $\tilde{l}_0 \tilde{e}_0$ and the surface tension using $\tilde{\rho}_0 \tilde{e}_0^2 \tilde{l}_0$. The relation of $\tilde{e}_0$ and $\tilde{\rho}_0$ to dimensional fluid constants, needed for practical applications, can be extracted from the state equation, as detailed in a forthcoming publication. The corresponding van der Waals constants are $a = 0.0273$ and $b = 0.225$, the interface thickness is $D = 3$ lattice units, the surface tension is $\sigma = 4.0 \times 10^{-4}$, and the grid size is $75 \times 75 \times 75$. Periodic boundary conditions have been employed in all principal directions. The pressure difference $P_{\mathrm{in}} - P_{\mathrm{out}}$ across the interface is calculated after a time period of about 25 000 time steps, which was required for the particle ensemble to reach equilibrium, and plotted against the droplet curvature in Fig. 2 (symbols). The straight line corresponds to Laplace's law for the prescribed surface tension ($\sigma = 4.0 \times 10^{-4}$):

$$\Delta P \equiv P_{\mathrm{in}} - P_{\mathrm{out}} = \frac{2\sigma}{R}. \tag{20}$$

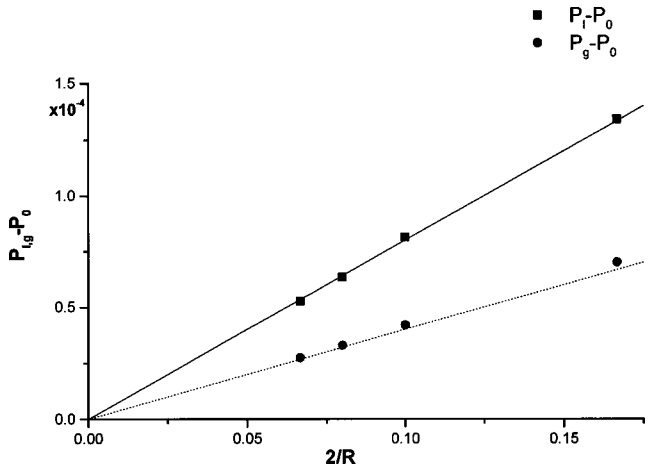

FIG. 3. Comparison of the simulated differences of liquid and vapor pressure in the equilibrated droplet case from the common pressure across a flat interface (symbols) with the predictions of the Gibbs-Thomson equations (solid lines).

Excellent agreement is observed between the prescribed and the calculated surface tension values.

A second validation test compares the liquid (P_l) and vapor (P_g) pressure values in the equilibrated droplet experiment to the prediction of the Gibbs-Thomson equations,

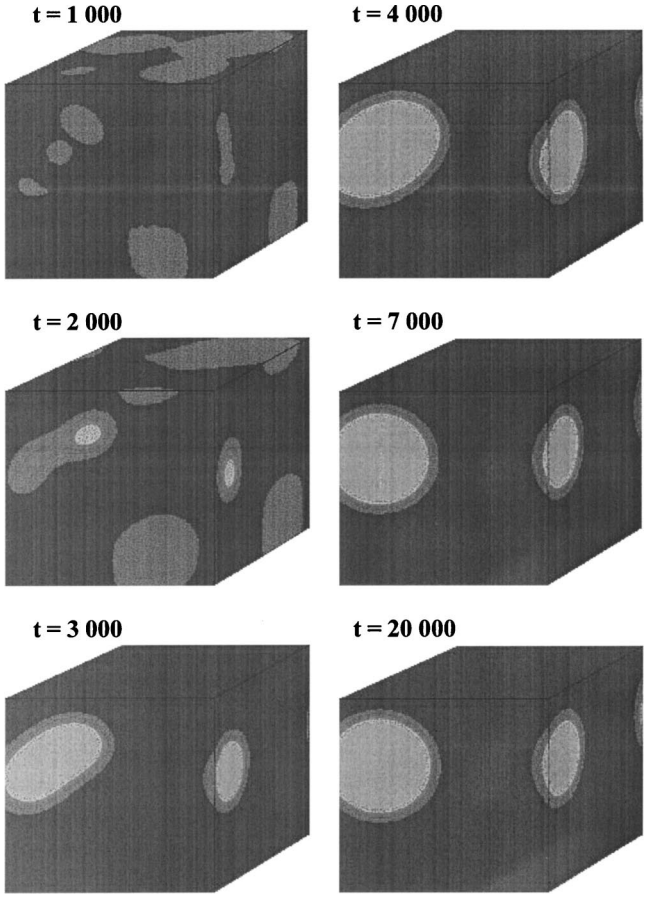

FIG. 4. Simulation of spinodal decomposition. Liquid fraction: 0.12.

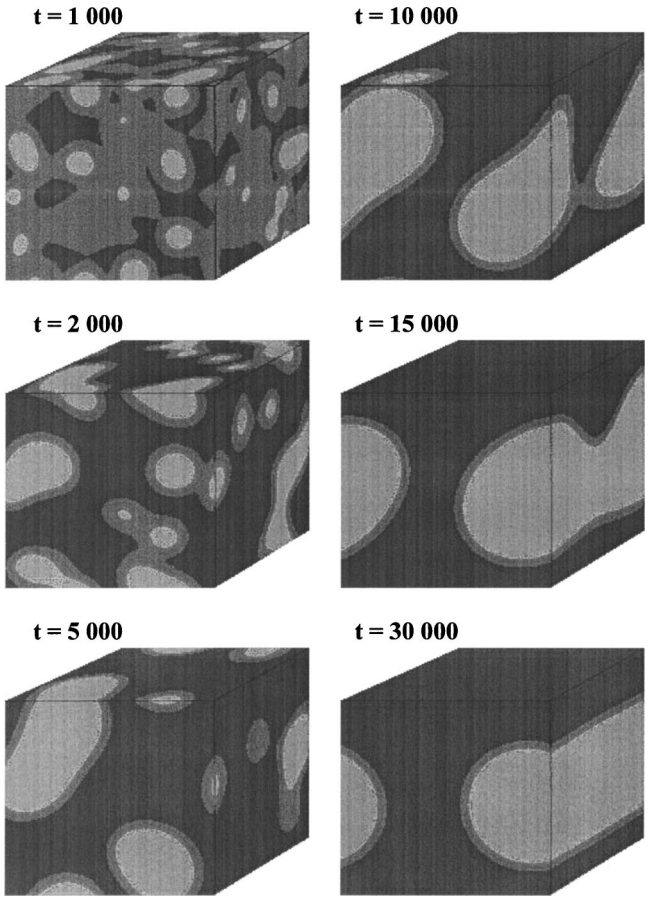

FIG. 5. Simulation of spinodal decomposition. Liquid fraction: 0.30.

$$P_g = P_0 + \left(\frac{\rho_g}{\rho_l - \rho_g}\frac{2}{R}\right)\sigma,$$
$$P_l = P_0 + \left(\frac{\rho_l}{\rho_l - \rho_g}\frac{2}{R}\right)\sigma, \tag{21}$$

where P_0 is the corresponding pressure for a flat interface. The parameter values are the same as those in the Laplace law test, namely, $\nu_l = \nu_g = 1.67\times10^{-2}$, $m = 1.8\times10^{-3}$, and $\rho_l = 2$, $\rho_g = 1$. Periodic boundary conditions have been employed around a $75\times75\times75$ grid. The system reached equilibrium after approximately 25 000 time steps. The aforementioned pressure differences are plotted as symbols in Fig. 3 against the droplet curvature. The dashed lines represent the theoretical values of the pressure differences, given by the Gibbs-Thomson equations for the prescribed surface tension ($\sigma = 4\times10^{-4}$). Again, a very good agreement between the simulated and the theoretical pressure difference values is observed.

Phase separation is simulated next. The working domain is filled initially with vapor and liquid particles, randomly distributed. Self-organization of particles is initiated by the local density gradients through the pressure tensor [Eq. (6)] at the interface. The action of the surface tension results in a single liquid body, the shape of which is a function of the initial density of the particle ensemble. Three different

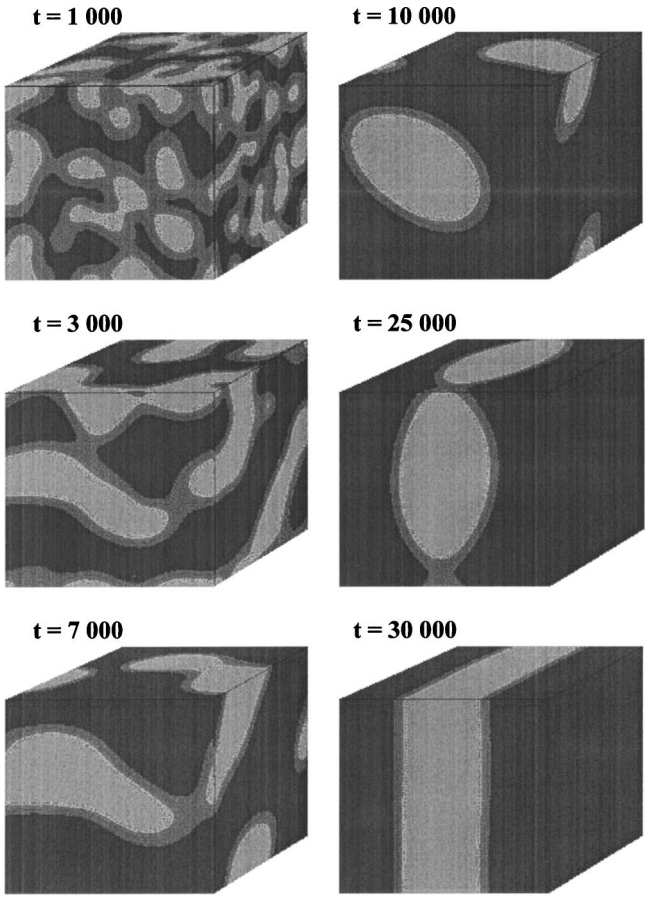

FIG. 6. Simulation of spinodal decomposition. Liquid fraction: 0.40.

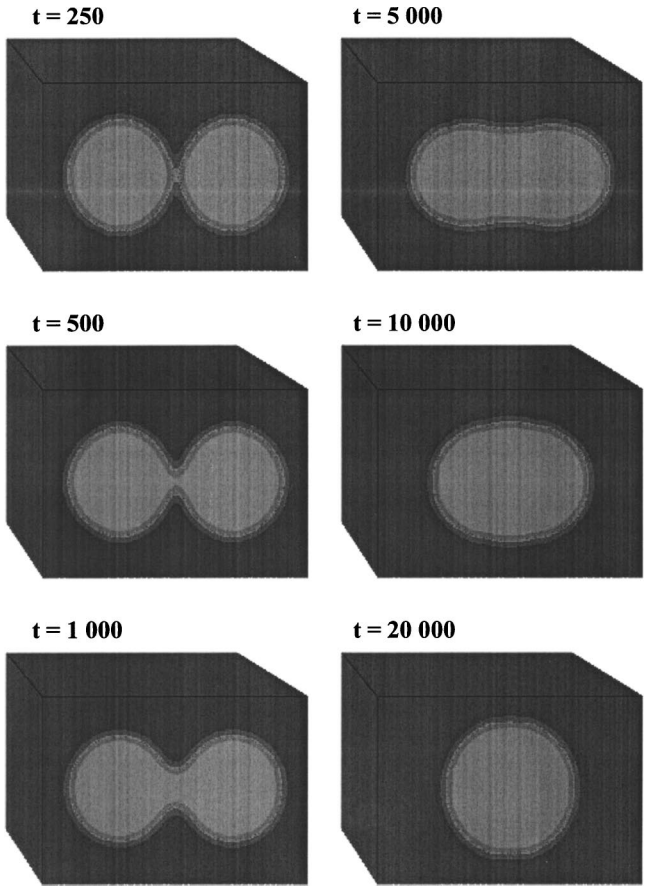

FIG. 8. Simulated snapshots of the coalescence of two liquid droplets.

shapes can be attained for periodic domains of finite size, as seen in Figs. 4–6. The parameter values in these simulations are $\nu_l=\nu_g=0.01$, $m=0.001$, $\rho_l=2$, and $\rho_g=1$, the corresponding surface tension is $\sigma=1.66\times10^{-4}$, and the grid size is $75\times75\times75$. The results are consistent with the analytical predictions of the minimal interfacial area for various values of the initial liquid fraction (Fig. 7).

Figure 8 shows simulated snapshots of the coalescence of two equally sized droplets. The parameter values are $\nu_l=\nu_g=0.01$, $m=2.5\times10^{-4}$, $\rho_l=2$, $\rho_g=1$, the corresponding surface tension is $\sigma=8.3\times10^{-5}$, and the grid size is $60\times40\times40$. If the droplets are brought sufficiently close so that their interface layers overlap, the density gradients that develop there trigger the formation of a liquid bridge between the droplets, followed by a gradual coalescence into a composite droplet, which eventually acquires spherical shape

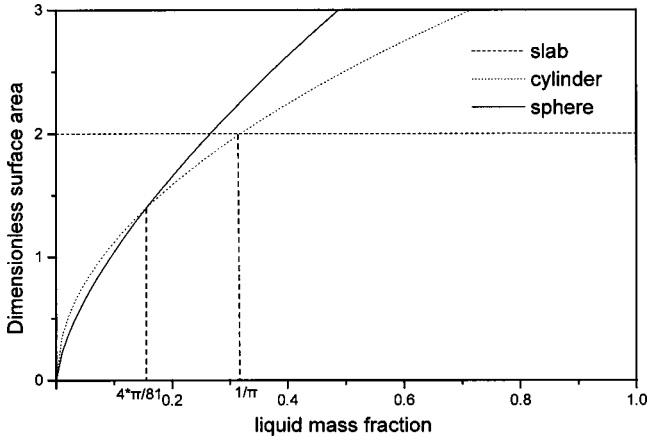

FIG. 7. Dependence of the shape of the minimum surface area of a periodic liquid-vapor system on the liquid fraction.

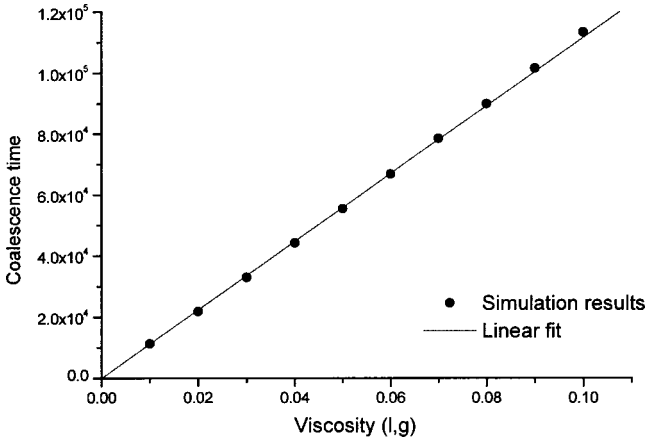

FIG. 9. Dependence of the coalescence time on the viscosity for two identical droplets brought into contact.

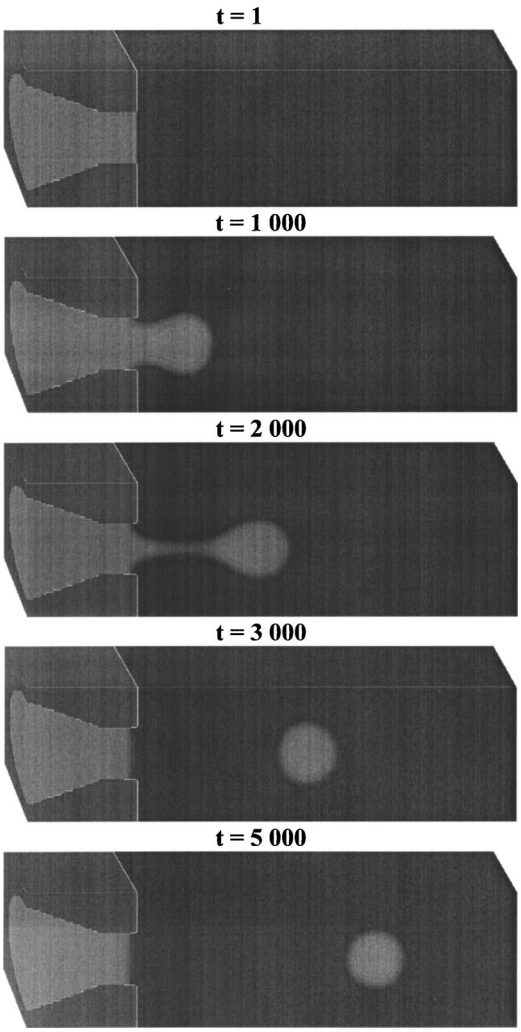

FIG. 10. Simulated snapshots of droplet generation from a conical orifice. $N_{\mathrm{Re}}=726$ at the liquid inlet.

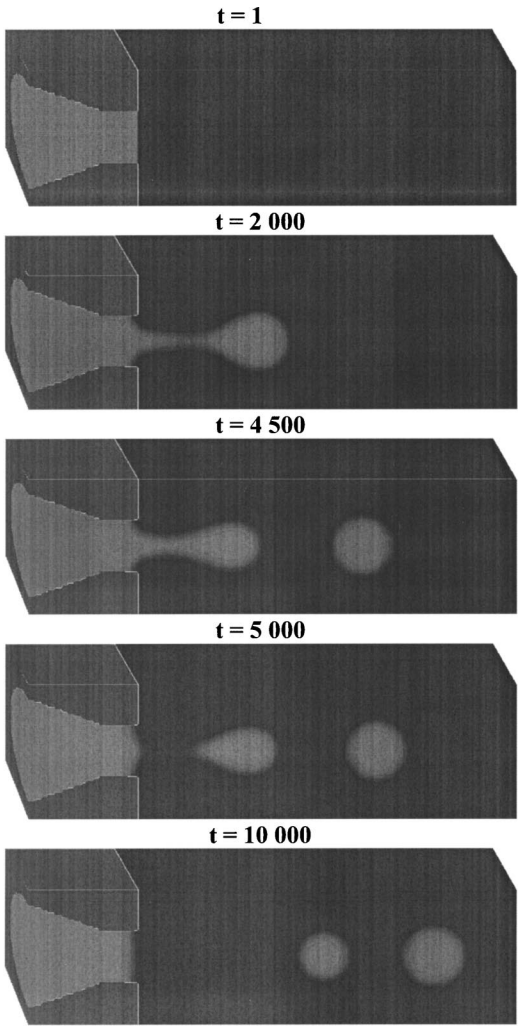

FIG. 11. Simulation of a sequential droplet generation from a conical orifice. First cycle: $N_{\mathrm{Re}}=653$; second cycle: $N_{\mathrm{Re}}=581$, at the liquid inlet.

owing to the surface tension. It should be noted that this behavior of spontaneous coalescence is observed in the case of droplets of a volatile liquid. If the liquid is not volatile, the behavior is quite different. The drops may need to be squeezed against each other for coalescence to take place.

The effect of the viscosity on the coalescence time, defined as the time needed for the completion of the mass transport process and equilibration to a spherical composite droplet, is shown in Fig. 9. The parameter values are $m=2.5\times10^{-4}$, $\rho_l=2$, $\rho_g=1$, the corresponding surface tension is $\sigma=8.3\times10^{-5}$, and the grid size is $60\times40\times40$. In this figure, a common value of the dynamic viscosity for the two phases was used as abscissa, keeping $\nu_g=2\nu_l$. The coalescence time follows a linear increase with viscosity, as expected [19,20]. It is noteworthy that in order to improve the accuracy of the calculation of the coalescence time, the simulations involved an initial stage, that allowed equilibration of the two droplets, kept sufficiently away from each other. The two droplets were then placed next to each other and allowed to coalesce.

In the presence of solid walls, two further boundary conditions must be defined, namely, the fluid velocity at the wall and the wettability or, equivalently, the contact angle at the liquid-vapor interface. The no-slip condition is used in this work, implemented through the simple bounce-back rule. The wettability condition is imposed by prescribing a chemical potential value at the wall, $\mu_w(r)$, that may be different from the bulk fluid one, thus introducing locally a chemical potential gradient that acts as an external force [2] at the wall-fluid interface. Alternatively, one can prescribe a density $\rho_w(r)$ at the wall sites, which corresponds to a chemical potential value through the equation

$$\mu(\rho,T)=kT\ln\frac{\rho}{1-b\rho}+\frac{kT}{1-b\rho}-2a\rho \tag{22}$$

for a van der Waals fluid [4].

The aforementioned conditions are employed in the simulation of jet formation out of a conical orifice, as shown in Fig. 10. The parameter values are $\nu_l=0.375$, $\nu_g=0.05$, $m=1.\times10^{-3}$, $\rho_l=10$, and $\rho_g=1$, the corresponding surface tension is $\sigma=1.54\times10^{-2}$, and the grid size is $60\times60\times200$. The diameter of the nozzle tip is 22 lattice units and

the nozzle length is 44 lattice units. Initially, the interior of the nozzle is filled with liquid, whereas the vapor density is assigned to every other fluid site. The nozzle is liquid wet ($\rho_w=\rho_l$) except for a narrow ring at the nozzle tip, of length equal to 3 lattice units, which is vapor wet ($\rho_w=\rho_g$).

Periodic boundary conditions are used in faces parallel to the jet direction. At the downstream exit face, it is assumed that the fluid velocity in the jet direction is no further varied with the distance form the nozzle ($\partial_z u_z=0$). At the liquid inlet, momentum is added to the boundary sites in the jet direction, the magnitude of which can be treated as a parameter, along with the viscosities, densities, and surface tension. This external force is applied for a finite-time interval and is subsequently discontinued for a fixed period of time. Then the charge stage is repeated again, followed by a rest period, and so on. Figure 10 shows simulated snapshots of such an operation, the charge period lasting 600 time steps and followed by a rest stage through the end of the cycle. If a shorter rest stage is used (1900 time steps), a second droplet can also be formed during the second cycle of operation, as shown in Fig. 11. In this particular case, the magnitude of the force applied during the second cycle is reduced to 0.8 of that employed in the first cycle, thus resulting in a smaller droplet, as expected.

IV. CONCLUSIONS

A 3D lattice Boltzmann model of nonideal fluids was developed, and simulations of liquid-vapor equilibrium and flow were performed. The model uses the van der Waals theory of nonuniform fluids and the Cahn-Hilliard formulation, adopted by Swift *et al.* [2] in their two-dimensional model. The continuity and Navier-Stokes equations are fully recovered, following a methodology similar to that described by the authors in a recent publication [1] that restored Galilean invariance in the 2D version of the model.

The 3D model was validated here under static conditions using simulations of droplet equilibrium and comparing pressure estimates to the prescription of the Laplace law and Gibbs-Thomson equations. Prescription of the parameter values was made possible though the algorithm presented by Angelopoulos *et al.* [4]. Spinodal decomposition and droplet coalescence were also simulated under a variety of parameter values. It was found that the droplet coalescence time increases linearly with the viscosity, in accord with similar literature findings.

The wettability of solid walls in jet simulations was adjusted through the prescription of a chemical potential profile or, equivalently, a fluid density profile at the wall-fluid interface. Droplet formation from an orifice was reproduced using both the momentum injection and the body force approaches. Sequential droplet generation was also achieved and the size of ejected droplets was found to decrease with decreasing applied force, as expected. Because of the ability of the simulator to reproduce directly the entire process of droplet formation and breakup, detailed studies of the fundamental transport phenomena and underlying mechanisms can be performed and a useful comparison with other numerical predictions can be made. Although the model presented here is ideally suited to treat two-phase systems with a moderate density ratio and relatively thick interface compared to the characteristic curvature radius, future work could be directed to relaxing these limitations and further widen the applicability of the method.

ACKNOWLEDGMENTS

This work was supported financially by the Institute of Chemical Engineering and High Temperature Chemical Processes—Foundation for Research and Technology (ICE/HT-FORTH), Hellas and by SEIKO-EPSON Corporation.

[1] A. N. Kalarakis, V. N. Burganos, and A. C. Payatakes, Phys. Rev. E **65**, 056702 (2002).
[2] M. R. Swift, W. R. Osborn, and J. M. Yeomans, Phys. Rev. Lett. **75**, 830 (1995).
[3] M. R. Swift, E. Orlandini, W. R. Osborn, and J. M. Yeomans, Phys. Rev. E **54**, 5041 (1996).
[4] A. D. Angelopoulos, V. N. Paunov, V. N. Burganos, and A. C. Payatakes, Phys. Rev. E **57**, 3237 (1998).
[5] J. S. Rowlinson and B. Widom, *Molecular Theory of Capillarity* (Clarendon, Oxford, 1982).
[6] J. W. Cahn and J. E. Hilliard, J. Chem. Phys. **28**, 258 (1958).
[7] D. J. Holdych, D. Rovas, J. G. Georgiadis, and R. O. Buckius, Int. J. Mod. Phys. C **9**, 1393 (1998).
[8] G. Házi, A. R. Imre, G. Mayer, and I. Farkas, Ann. Nucl. Energy **29**, 1421 (2002).
[9] X. He, X. Shan, and G. D. Doolen, Phys. Rev. E **57**, R13 (1998).
[10] X. He, S. Chen, and R. Zhang, J. Comput. Phys. **152**, 642 (1999); X. He, R. Zhang, S. Chen, and G. D. Doolen, Phys. Fluids **11**, 1143 (1999).
[11] N. Takada, M. Misawa, A. Tomiyama, and S. Fujiwara, Comput. Phys. Commun. **129**, 233 (2000).
[12] R. R. Nourgaliev, T. N. Dinh, and B. R. Sehgal, Fusion Eng. Des. **211**, 153 (2002).
[13] P. L. Bhatnagar, E. P. Gross, and M. Krook, Phys. Rev. **94**, 511 (1954).
[14] S. Wolfram, J. Stat. Phys. **45**, 471 (1986).
[15] Y. Qian, D. d'Humieres, and P. Lallemand, Europhys. Lett. **17**, 479 (1992).
[16] R. Evans, Adv. Phys. **28**, 143 (1979).
[17] B. T. Nadiga and S. Zaleski, Eur. J. Mech. B/Fluids **15**, 885 (1996).
[18] Q. Zou and X. He, Phys. Rev. E **59**, 1253 (1999).
[19] D. E. Siggia, Phys. Rev. A **20**, 595 (1979).
[20] C. Andrieu, D. A. Beysens, V. S. Nikolayev, and Y. Pomeau, J. Fluid Mech. **453**, 427 (2002).